

Automated Image Analysis of Hodgkin lymphoma

Alexander Schmitz¹, Tim Schäfer¹, Hendrik Schäfer¹, Claudia Döring², Jörg Ackermann¹, Norbert Dichter¹, Sylvia Hartmann², Martin-Leo Hansmann², and Ina Koch¹

¹Institute of Computer Science, Department of Molecular Bioinformatics, Johann Wolfgang Goethe-University Frankfurt (Main), Robert-Mayer-Strasse 11–15, 60325 Frankfurt (Main), Germany, ina.koch@bioinformatik.uni-frankfurt.de

²Senckenberg Institute of Pathology, Johann Wolfgang Goethe-University Frankfurt (Main), 60590 Frankfurt (Main), Germany, m.l.hansmann@em.uni-frankfurt.de

November 11, 2021

Abstract

Motivation: Hodgkin lymphoma is an unusual type of lymphoma, arising from malignant B-cells. Morphological and immunohistochemical features of malignant cells and their distribution differ from other cancer types. Based on systematic tissue image analysis, computer-aided exploration can provide new insights into Hodgkin lymphoma pathology.

Results: In this paper, we report results from an image analysis of CD30 immunostained Hodgkin lymphoma tissue section images. To the best of our knowledge, this is the first systematic application of image analysis to a set of tissue sections of Hodgkin lymphoma. We have implemented an automatic procedure to handle and explore image data in Aperio's SVS format. We use pre-processing approaches on a down-scaled image to separate the image objects from the background. Then, we apply a supervised classification method to assign pixels to predefined classes. Our pre-processing method is able to separate the tissue content of images from the image background. We analyzed three immunohistologically defined groups, non-lymphoma and the two most common forms of Hodgkin lymphoma, nodular sclerosis and mixed cellularity type. We found that nodular sclerosis and non-lymphoma images exhibit different amounts of CD30 stain, whereas mixed cellularity type exhibits a large variance and overlaps with the other groups. The results can be seen as a first step to computationally identify tumor regions in the images. This allows us to focus on these regions when performing computationally expensive tasks like object detection in the high-resolution image.

Contact: ina.koch@bioinformatik.uni-frankfurt.de, m.l.hansmann@em.uni-frankfurt.de

1 Introduction

In this paper, we describe the analysis of tissue image data of Hodgkin lymphoma using computational methods.

1.1 Hodgkin lymphoma

Hodgkin lymphoma (HL) is a type of lymphoma, originating from B-cells in most of the cases [13]. In HL, neoplastic cells circumvent the immune surveillance and apoptotic control. A key characteristic in HL is that the malignant cells make up only about 1% of the tumor mass, while being outnumbered by a microenvironment of reactive lymphoid cells [26, 16]. Depending on

the infiltrate, morphological, phenotypic, genotypic, and clinical findings, HL is further subdivided. According to the WHO classification, the main subtypes are classical HL (cHL) and nodular lymphocyte-predominant HL (NLP HL).

The assignment to cHL is based on the identification of characteristic tumor cells. These cells are termed Hodgkin and Reed-Sternberg cells (HRS cells) [22, 27]. For immunophenotypic differentiation of HL, methods from the field of immunohistochemistry are used. Of particular interest for this work are the cluster-of-differentiation protocols (CD), used to identify cell surface proteins presented on leukocytes (e.g., CD30, CD20, CD15). CD30 belongs to the tumor necrosis receptor family (TNFR) and is usually expressed by HRS cells. Figure 1 illustrates a typical CD30⁺ immunostained HRS cell within its microenvironment. Hematoxylin counterstaining is applied to visualize cell nuclei. cHL is further divided into subtypes depending on immunophenotypic findings and the composition of the cellular microenvironment; the most common subtypes are termed nodular sclerosis (NS cHL), and mixed cellularity (MC cHL) [8]. All subtypes of cHL share an immunophenotype of CD30⁺, CD15⁺, and CD20⁻ [12].

Moreover, the expression of various cytokines and chemokines is thought to be responsible for the attraction of different cells, such as small lymphocytes, macrophages, mast cells, plasma cells, stromal cells, histiocytes, or fibroblasts [2, 26]. The extent of cellular infiltration, involving many different cell types as a response to inflammatory signals, represents a key characteristic of HL. The events that happen in the course of malignancy development as well as the complex interaction network of malignant cells in HL remain to be resolved. This can be done using image processing, which may provide new insights into the pathology of HL.

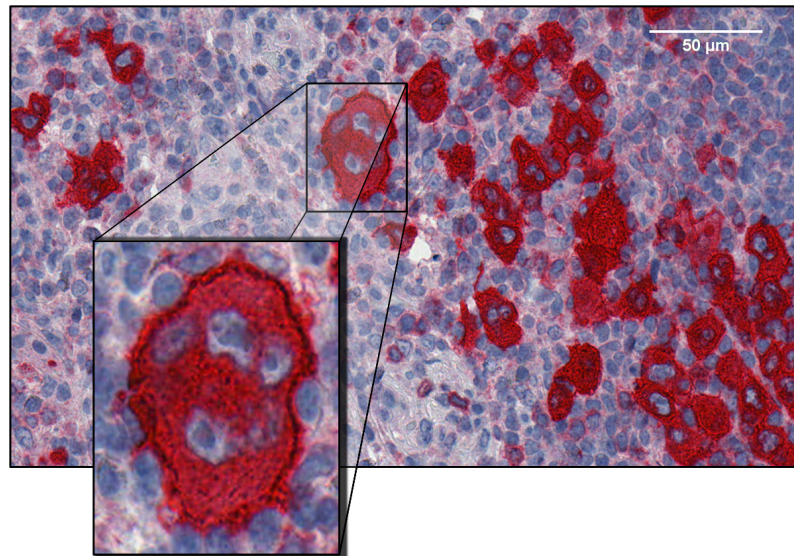


Figure 1: **CD30⁺ Reed-Sternberg cell.** Malignant cells are marked with CD30 immunostain. Additional hematoxylin counterstain is provided to visualize nuclei. A giant RS cell can be seen in the center of the image, outnumbered by a variety of other lymphoid cells (nuclei are visible). Multiple irregularly shaped nuclei are visible, a distinguishing feature of this cell.

1.2 Whole Slide Image Analysis

There is a broad range of literature on image analysis of non-lymphoid tumors. Automated methods for the analysis of histology images have been employed in various cancer types to detect, classify,

and quantify cells. A common issue is the segmentation of cell nuclei. For instance, Naik *et al.* used a Bayesian nuclear segmentation scheme in prostate and breast cancer histopathology, integrating color, texture, and shape information [19]. Bayesian models with additional contextual information from Markov random fields have been applied as a probabilistic approach for prostate cancer detection [18]. More general approaches for hematoxylin & eosin (H&E) stained images have also been applied. Lei *et al.* used Gaussian mixture models to perform local and global clustering, extracting different tissue constituents in cervix histology images [15]. Sertel *et al.* developed a system for segmentation of eosinophilic and basophilic structures in H&E stained tissue section images of neuroblastoma. Different tissue subtypes were classified using texture features and a new set of structural features [24].

Large-scale computations and machine learning algorithms have been applied to breast histology images [21]. A hybrid segmentation approach and supervised classification scheme have been used to identify micro-textures meaningful for differentiation of tissue types. Karacali *et al.* proposed a high-throughput method of texture heterogeneity on breast tissue images to identify regions of interest. They subdivide the images into small image blocks and pass these blocks to a texture-based statistical learning algorithm, which classifies them into categories of normal, malignant, and non-specific tissue [11].

Some investigations were performed on non-Hodgkin lymphoma. An automatic classification of three types of malignant lymphoma has been proposed by Orlov *et al.*, taking into account chronic lymphocytic leukemia, follicular lymphoma (FL), and mantle cell lymphoma [20]. The classification is based on a supervised classifier (WND-CHARM), applying additional feature weights learned in the classifier's training phase. They achieved high accuracy in discriminating the different lymphoma types using various statistical and texture features. FL arises from the malignancy of follicle center B cells. Sertel *et al.* developed a computerized system to detect follicles based on texture features in an immunostained image. This is followed by the detection of centroblasts within the follicular regions [25].

Today, a number of software solutions for analyzing images is available. Commercial software includes general tools like MATLAB [17] as well as software geared especially towards digital pathology like Aperio ImageScope [10], Definiens Tissue Studio [3], and many other. There exist also freely available tools, the most prominent of which are CellProfiler [14], ImageJ [1], GNU Octave [4], and Scilab [23].

Despite all these approaches, no work exists for HL. NS CHL (nodular sclerosis) and MC CHL (mixed cellularity) represent two different types of HL which often have distinct patterns of tumor cell distribution. In NS CHL, the tumor cells grow in a nodular pattern with broad collagen bands separating the nodules. In contrast, MC CHL tumor cells are more isolated and often distributed over the whole tissue section. NS CHL accounts for about 64%, whereas MC CHL is found in about 30% of the CHL cases. While the visual differentiation between the two types of CHL is possible in many cases, non-lymphoma images sometimes exhibit features similar to CHL subtypes. An example is lymphadenitis, an infection of the lymph nodes, which may result from certain bacterial infections and often leads to inflammation and swelling of lymph nodes.

Our goal is to analyze the considered types based on CD30 stained tissue sections, using pixel based image processing techniques. We use our own implementation to be flexible in handling and exploring HL whole slide tissue-images and to easily extend the software in future projects. Our software is intended to evolve into a tool that extracts statistical information from a large database of Hodgkin lymphoma images. It will be combined with existing imaging software solutions like CellProfiler [14].

2 Material

The source images used in this study are CD30 stained tissue slides of lymph node sections. The tissue sections have been pretreated, and immunostainings for CD30 were performed as described previously [9]. Hematoxylin counterstain was applied to stain cell nuclei. The slides were assigned by pathologists to one of the following groups:

- Nodular sclerosis classical Hodgkin lymphoma (NS cHL)
- Mixed cellularity classical Hodgkin lymphoma (MC cHL)
- Non-lymphoma (lymphadenitis with and without follicular hyperplasia)

All samples were randomly taken from an anonymized data set from the *Senckenberg Institute of Pathology Frankfurt am Main*. Tissue sections of small size may not be representative for the complete lymph node and were discarded. Furthermore, only tissue sections with distinct immunostaining were taken into account. In these images, CD30⁺ cells can be visually distinguished from the background. This selection has been carried out by pathologists yielding 62 images of NS cHL, 57 of MC cHL, and 51 of non-lymphoma.

The digital slides were captured using an *Aperio ScanScope XT* scanning device with a 40x objective lens. The typical size of the tissue samples is about 15 mm², and the resulting images reach dimensions of up to 100,000 x 100,000 pixels (0.25 μ m per pixel). The images are provided in the Aperio SVS format, a single-file pyramidal TIFF with non-standard metadata and compression. Our input files contain four levels with different resolutions of the original image, each of which is split into tiles. For our analysis, we use the second level which is down-scaled by a factor of 16 on each axis compared to the full-resolution image.

3 Methods

We use OpenSlide 3.2 to handle whole slide images and implement our analysis applying the Java Advanced Imaging API [6]. The input images contain stained tissue in front of a bright background. They may also include artifacts like air bubbles, small tissue fragments and stain residues. To eliminate such artifacts, as well as background, we apply image pre-processing steps.

3.1 Pre-Processing

During pre-processing, we use Gaussian filtering, thresholding, and region labeling to identify the tissue region as described in [5]. We analyze the tissue region in the following classification steps.

Gaussian filtering We convolve the input image with a Gaussian filter which is applied to all three RGB channels. This step blurs the input image by replacing the RGB values of each pixel by the weighted RGB values of a 43×43 window. The weights follow a Gaussian distribution with a variance of $\sigma = 3$ pixels. The images are prepared for the threshold process by filtering. Thereby, pixels inside the tissue area are kept from falling into the background category.

Threshold background pixels The usage of a threshold becomes feasible since all images share a distinct background peak in the histogram. We convert the images to gray scale by averaging the RGB values of the three channels and then split the histogram of the resulting image into two distinct classes by choosing a threshold value. Thus, pixels are labeled as either object or background pixels during this process. A threshold is applied to the smoothed image using the

brightness value of the local minimum next to the background peak. Pixels labeled as background are removed from the original image whereas those of tissue regions are retained.

Filtering tissue regions The remaining pixels can be separated into connected areas using a region labeling method. Connected areas correspond to pixel regions, such that a connecting path exists between each pair of pixels. The region labeling algorithm identifies all connected regions within the image. Only pixels belonging to a sufficiently large area are retained. We choose a region size of 40,000 pixels as threshold. This results in discarding small separated tissue fragments and spots on the object slide. Figure 2 demonstrates an example for the effects of these three pre-processing steps.

3.2 Pixel Classification

We use the following terminology: all images assigned by pathologists to the same type (NS CHL, MC CHL or NL) are called a *group*. During pixel classification, pixels are assigned to one of the *pixel classes* defined in this section.

After pre-processing, the pixels considered as tissue are classified using a supervised approach. For each pixel, a set of descriptors is computed as signature. We apply a minimum distance classifier, which is trained on examples for each pixel class, resulting in one mean signature, a vector of descriptor values. Therefore, we manually prepared a set of 36 image sections which represent the pixel classes (6 images per class, image size between 150 and 1000 pixels). The classifier assigns a pixel to the reference pixel class whose signature is closest to the pixel’s signature. To compute the distance between pixel class and a sample signature a predefined Euclidean distance measure is applied. The mean signatures for the following pixel classes are determined:

- **Background:** The pre-processing does not eliminate all pixels that may be assigned to background. Therefore, the class *Background* represents such pixels.
- **Low intensity:** Pixels having very low intensity should also be regarded as non-tissue.
- **Hematoxylin⁺:** Cell nuclei are hematoxylin positive and stained in deep blue.
- **CD30⁺:** CD30⁺ stained regions are typical for RS cells. Thus, CD30 is an indicator for possible tumor cells.
- **Nonspecific red:** These are image regions which are colored red, but not due to CD30 staining. Examples include prolate regions resembling vessels.
- **Unstained:** Nonspecifically stained regions are slightly colored.

To compute the signature we use a set of low-level pixel-based descriptors. All descriptors are solely based on the pixel intensity values. The set of descriptors is defined as follows:

- **Brightness Descriptor:** The mean value over all three color channels red (R), green (G), and blue (B) of a considered pixel is computed.
- **Mean Descriptor:** For all pixels within a distance of one pixel using an 8-connected neighborhood, we take the average values of the R, G, and B channels.
- **CD30 Saturation:** To account for the CD30 staining, we use a modified saturation descriptor, which is given in Equation 1. We only consider two stainings which are red and blue, so green pixels can only be produced by artifacts or noise.

$$S_{CD30} = (\max(|R - B|, |R - G|) - \min(|R - B|, |R - G|, |B - G|)) \quad (1)$$

Finally, we compute the number of pixels which have been assigned to the defined pixel classes for each image. This results in a vector for each image containing the pixel counts for each pixel class. The counts of *Unstained*, $CD30^+$, *Nonspecific red*, and *Hematoxylin*⁺ represent the tissue classes. Since we are interested in the tissue classes, we omit the counts of *Background* and *Low intensity*. For the tissue classes, we compute the fraction of total pixels belonging to the respective class.

4 Results and Discussion

The pre-processing steps are able to identify regions of interest and discard background information. Figure 2 depicts an example for the effects of the pre-processing. As visible in Box 1, background pixels are rejected. Furthermore, tissue fragments and connective tissue areas are also ignored (Box 2).

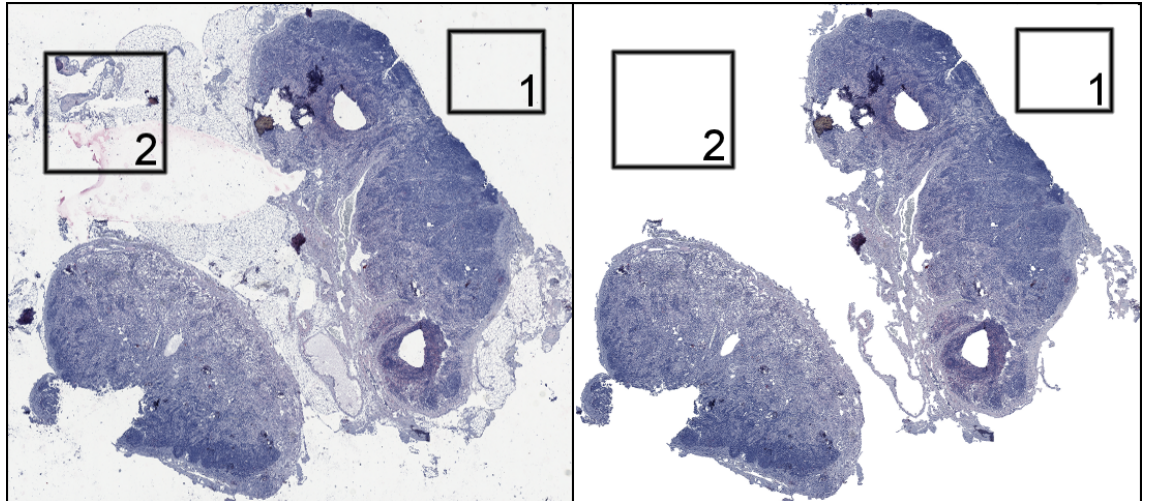


Figure 2: **Pre-processing steps applied to example tissue slide.** Comparison of tissue section before (left) and after (right) the pre-processing step. The image is first processed using Gaussian filtering. Background thresholding, followed by a region labeling algorithm is then applied to remove fragments and small particles, which may occur during the preparation process. In Box 1, the removal of background pixels is illustrated. Box 2 depicts the elimination of tissue fragments and connective tissue.

The pixel classes referred to in this paper reflect one way of describing the content of histological images. These classes were found to give reasonable results for the underlying image data. For a more detailed view, Figure 3 depicts the results of pixel-based classification for small image regions. On the top, the original image region is shown, whereas on the bottom the resulting image is depicted. Images A and B demonstrate that $CD30^+$ regions are correctly assigned in most of the cases. Moreover, *Unstained* and *Hematoxylin*⁺ regions are separated from each other. The class *Low intensity* is introduced to primarily cover areas, where tissue folds and disruptions occur. In such areas, it is difficult to assign pixels to tissue classes. Therefore, we want to exclude these areas altogether. For instance, Figure 3C contains an area of disrupted tissue. Pixels within this region have low intensity values. As visible in Figure 3D, the classifier assigns most of these pixels to the class *Low intensity*. In Figure 3E, a red area without distinct $CD30$ staining is visible. Pixels within this region are mostly assigned to *Nonspecific red*. From these figures it can be

inferred that the pixel-based classification is able to identify the supplied training classes based solely on color information. This could be also confirmed by visual examination of the resulting images.

The results of the pixel classification allow us to identify image regions containing $CD30^+$ cells. As $CD30$ is a marker for HRS cells, information on these sections can be used to quickly select regions in the full-resolution level of the images, where candidates for HRS cells exist. To filter the images for these regions of interest, we apply a grid which subdivides the image into tiles of size 32×32 pixels, which corresponds to an area of 512×512 pixels in the full-resolution image. Then, we discard all tiles which do not contain any $CD30^+$ pixel, see Figure 4. In Figure 4B, we see that a large amount of tiles does not contain candidate $CD30^+$ cells. For the whole image, about 75% of the tiles could be ignored. This substantially reduces the computational costs of further processing steps, e.g., object detection in the full-resolution image.

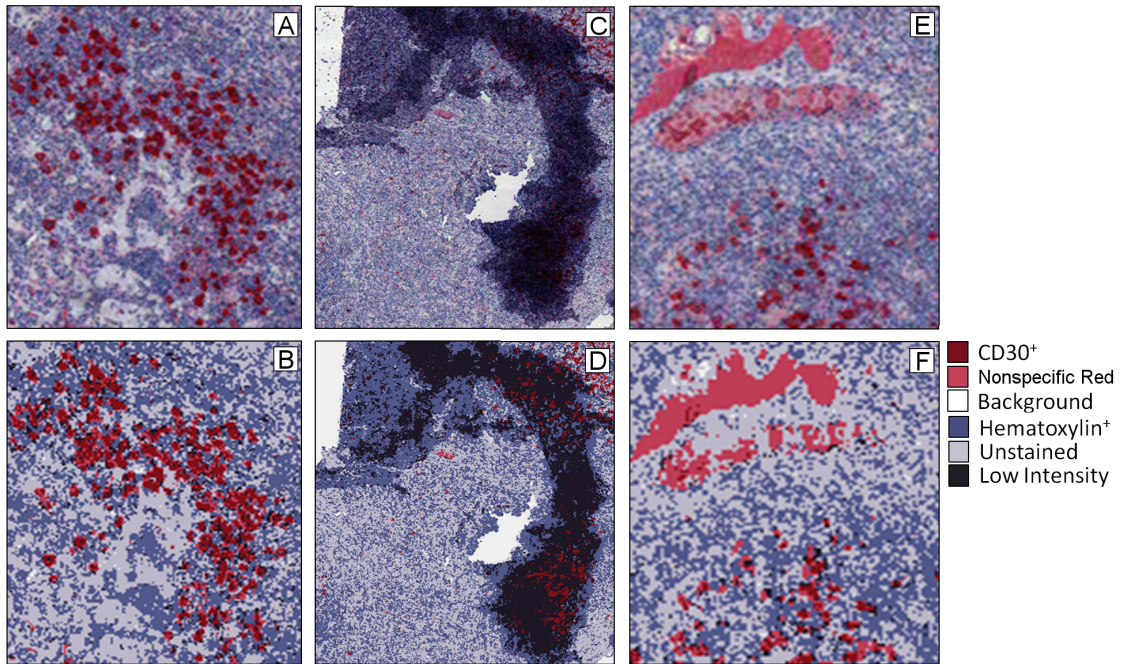
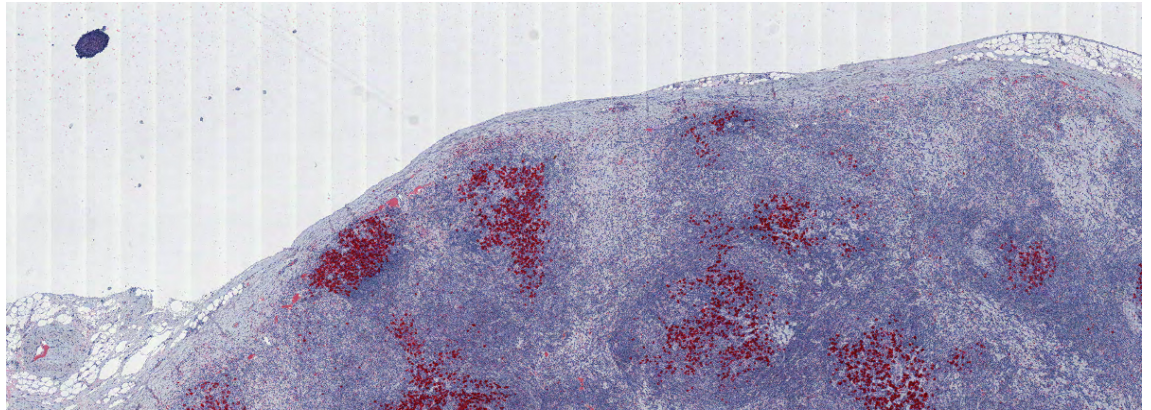


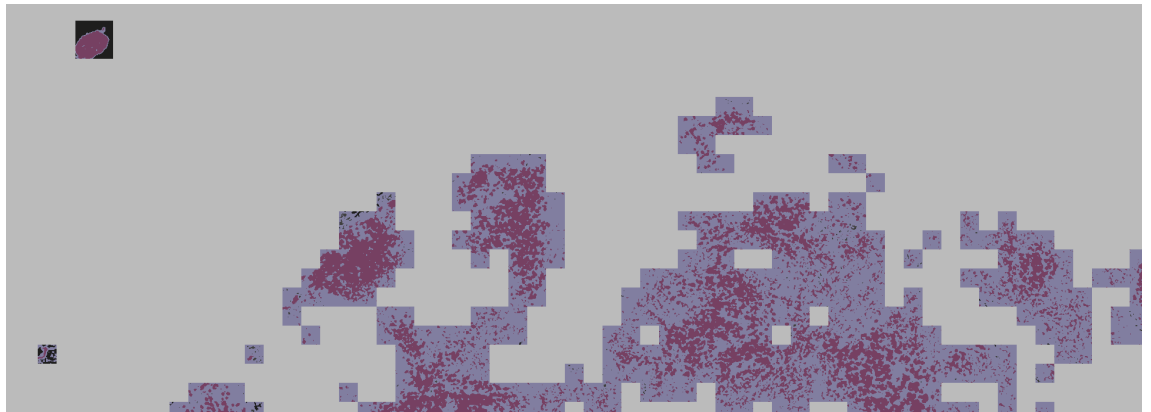
Figure 3: Detailed view of classified image sections. Images A and B depict the classification results for $CD30^+$ regions. In C and D, the classification results for areas with tissue folds are depicted. E and F present the distinction between $CD30^+$ and *Nonspecific red*.

The quantification results for non-lymphoma, NS cHL, and MC cHL are depicted in Figure 5. The relative amount of $CD30^+$ pixels in non-lymphoma cases is considerably lower than in NS cHL and MC cHL, see Figure 5A. This is expected because $CD30^+$ Hodgkin and RS cells are a characteristic feature of cHL. However, small amounts of $CD30^+$ cells are known to occur in non-lymphoma cases and can be visually confirmed in the source images.

The amount of $CD30^+$ in the groups is proportional to the amount of *Nonspecific red*, due to the fact that the signatures of these groups are very similar. We use down-scaled versions of the original images, so a single pixel represents several pixels of the full-resolution image. Therefore, pixels at the borders of $CD30^+$ regions are averaged with their neighbors and may thus be classified as *Nonspecific red*. Nevertheless, visual inspection of the resulting images suggests that most of the red-colored regions without $CD30$ staining are correctly assigned to this pixel class.



(A) Section of an NS CHL example image.

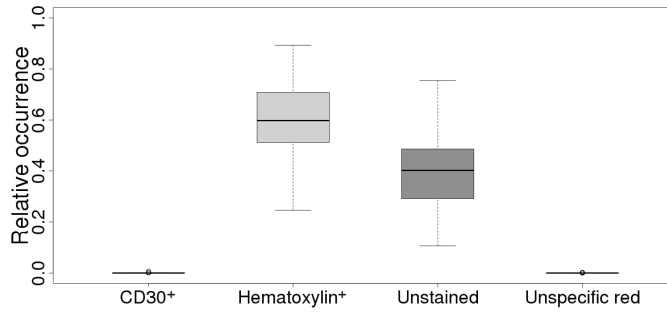


(B) Region of interest based on the pixel-classified image.

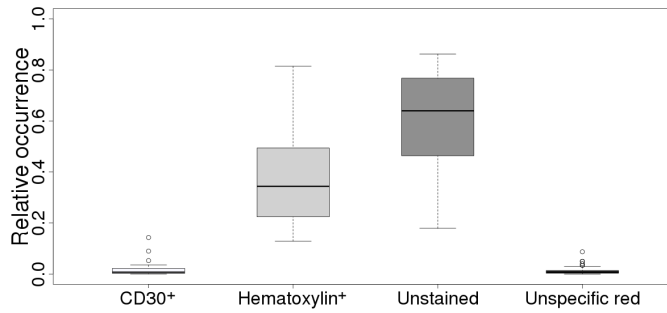
Figure 4: Results of region of interest identification in whole slide images. The pixel-classified image is reduced to the region of interest containing $CD30^+$ areas. Only tiles of the original image which contain possible $CD30^+$ cells are kept, tiles without $CD30^+$ regions are gray.

The number of pixels classified as *Hematoxylin*⁺ in tissue regions is rather low in NS CHL (compare Figure 5B). *Hematoxylin*⁺ can be understood as a label for regions with a high density of cell nuclei. The low number may correspond to the high amount of fibrotic bands occurring in this type of CHL. Figure 5C illustrates that the distributions for the pixel classes of MC CHL have a clear overlap with both other groups.

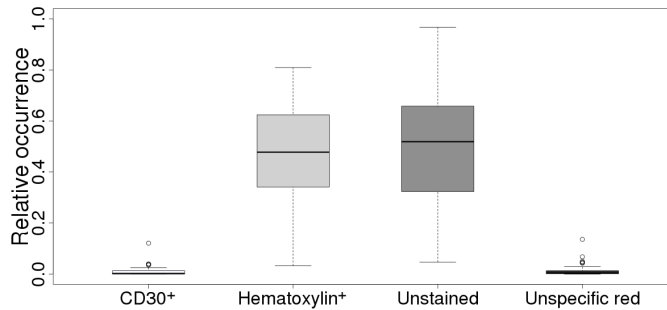
In conclusion, this suggests that all three groups contain images which are hard to classify by only considering their $CD30^+$ share. Due to the large overlap with both other groups, we assume that MC CHL is hard to distinguish from NL, and NS CHL. This assumption has been confirmed by an image classification approach using a minimum distance to mean classifier [5]. The classifier is based on the amount of $CD30^+$ pixels only. 50.6% of the images were classified correctly (NS CHL: 34/62, MC CHL: 26/57, NL: 26/51). This is an enrichment of 51.8% compared to a random draw, which would yield 33.33% correct assignments. It becomes apparent that pixel-based classification does not stand up to the current state-of-the-art approaches in image classification, as more sophisticated methods are reported to reach correct classification rates of up to 96% for similar images [7].



(A) Quantification results for non-lymphoma tissue sections.



(B) Quantification results for NS CHL tissue sections.



(C) Quantification results for MC CHL tissue sections.

Figure 5: Quantification results for non-lymphoma, NS CHL, and MC CHL tissue sections. The results present the relative amount of pixels which have been assigned to the tissue classes. $CD30^+$, $Hematoxylin^+$, *Nonspecific red*, and *Unstained* are considered as belonging to tissue. Pixels assigned to either the class *Background* or *Low Intensity* are taken together as non-tissue (not shown). For each class, the frequencies are averaged over all considered cases of non-lymphoma, NS CHL, and MC CHL, respectively.

5 Conclusion

In this work, we presented results of our automated image analysis applied to lymph node image data. To the best of our knowledge, there does not yet exist a systematic application of image analysis to HL. Standard pre-processing methods like Gaussian filtering, application of a threshold for background elimination and region labeling for identification of relevant tissue patches, were applied.

After pre-processing, a supervised classification was used to assign each pixel to one of the pixel classes: *Background*, *Low intensity*, *Unstained*, *CD30⁺*, *Hematoxylin⁺*, and *Nonspecific red*. For the quantification, we consider only tissue classes, i.e., pixels classified as *Unstained*, *CD30⁺*, *Hematoxylin⁺*, or *Nonspecific red*. For each pixel class, we computed the relative fraction of pixels belonging to the respective class.

We observed a large variation concerning the occurrences of pixel classes in the groups. This variation could be related to the large amount of images in each group and the fact that various stages of HL and different types of non-lymphoma cases were investigated. In advanced stages of HL disease, the amount of CD30⁺ cells increases whereas in early stages only few malignant cells can be detected. This may lead to statistical outliers within the groups.

Visual inspection of the images indicates that the spatial distribution of CD30⁺ cells differs between the image groups. For instance, in NS cHL the CD30⁺ cells are arranged in a nodular pattern whereas in most cases of MC cHL or NL CD30⁺ cells seem to be equally distributed over the entire tissue section. Therefore, we conclude that the usage of descriptors that include spatial information and additional tissue classes will improve the classification results. We intend to apply such descriptors using a combination of our software and existing implementations, like CellProfiler.

Because malignant cells in HL contribute only a small proportion of about 1% of the total cell count, large regions exist in the images which do not contain any HRS cell. The tile-based filtering approach addressed in Figure 4 may thus contribute to reduce computational cost of subsequent processing steps. In the near future, we plan to extend our approach by further analysis methods to gain high-level information from the image data which can then be used to address questions in systems biology.

References

- [1] M.D. Abramoff, P.J. Magalhaes, and S.J. Ram. Image processing with imageJ. *Biophotonics International*, 11, 2004.
- [2] D. Aldinucci, A. Glohini, A. Pinto, R. De Filippi, and A. Carbone. The classical Hodgkin's Lymphoma microenvironment and its role in promoting tumour growth and immune escape. *Journal of Pathology*, 221:248–263, 2010.
- [3] Definiens. Definiens tissue studio 3, 2012. Online; accessed 24 May 2012.
- [4] John W. Eaton, David Bateman, and Søren Hauberg. *GNU Octave Manual Version 3*. Network Theory Limited, 2008.
- [5] R. C. Gonzalez and R. E. Woods. *Digital Image Processing*. Prentice Hall International, 2007.
- [6] A. Goode and M. Satyanarayanan. A vendor-neutral library and viewer for whole-slide images. Technical report, Computer Science Department, Carnegie Mellon University, 2008.
- [7] M. N. Gurcan, L. E. Boucheron, A. Can, A. Madabhushi, N. M. Rajpoot, and B. Yener. Histopathological image analysis: A review. *IEEE Reviews in Biomedical Engineering*, 2:147–171, 2009.

- [8] M.-L. Hansmann and K. Willenbrock. Die WHO-Klassifikation des Hodgkin-Lymphoms und ihre molekularpathologische Relevanz. *Der Pathologe*, 23:207–218, 2002.
- [9] S. Hartmann, C. Agostinelli, W. Klapper, P. Korkolopoulou, K. Koch, T. Marafioti, P. P. Piccaluga, E. Patsouris, S. Pileri, and M.-L. Hansmann. Revising the historical collection of epithelioid cell-rich Lymphomas of the Kiel lymph node registry: what is Lennert’s Lymphoma nowadays? *Histopathology*, 59:1173–1182, 2011.
- [10] Aperio Technologies Inc. Aperio imagescope, 2011. Online; accessed 24 May 2012.
- [11] B. Karacali and A. Tözeren. Automated detection of regions of interest for tissue microarray experiments: an image texture analysis. *BMC Medical Imaging*, 7(2), 2007.
- [12] R. Küppers. The biology of Hodgkin’s Lymphoma. *Nature Reviews Cancer*, 9:15–27, 2009.
- [13] R. Küppers, K. Rajewsky, M. Zhao, G. Simons, R. Laumann, R. Fischer, and M.-L. Hansmann. Hodgkin disease: Hodgkin and Reed-Sternberg cells picked from histological sections show clonal immunoglobulin gene rearrangements and appear to be derived from B cells at various stages of development. *Proceedings of the National Academy of Sciences*, 91:10962–10966, 1994.
- [14] M.R. Lamprecht, D.M. Sabatini, and A.E. Carpenter. Cellprofiler: free, versatile software for automated biological image analysis. *Biotechniques*, 42, 2007.
- [15] H. Lei, S. Antani, and G. R. Thoma. Multiphase level set model with local k-means energy for histology image segmentation. In *Healthcare Informatics, First IEEE International Conference on Imaging and Systems Biology (HISB)*, pages 32–39, 2011.
- [16] S. Mathas, B. Dörken, and M. Janz. Die molekulare Pathogenese des klassischen Hodgkin Lymphoms. *Deutsche Medizinische Wochenschrift*, 134:1944–1948, 2009.
- [17] The Mathworks. Matlab, 2011. Online; accessed 24 May 2012.
- [18] J. Monaco, J. E. Tomaszewski, M. D. Feldman, M. Moradi, P. Mousavi, A. Boag, C. Davidson, P. Abolmaesumi, and M. Anant. Probabilistic pairwise Markov models: Application to prostate cancer detection. In *Proceedings SPIE Medical Imaging*, volume 7259, 2009.
- [19] S. Naik, S. Doyle, S. Agner, A. Madabhushi, M. Feldman, and J. Tomaszewski. Automated gland and nuclei segmentation for grading of prostate and breast cancer histopathology. In *5th IEEE International Symposium on Biomedical Imaging from Nano to Macro, ISBI 2008*, pages 284–287, 2008.
- [20] N. V. Orlov, W. W. Chen, D. M. Eckley, T. J. Macura, L. Shamir, E. S. Jaffe, and I. G. Goldberg. Automatic classification of Lymphoma images with transform-based global features. *IEEE Transactions on Information Technology in Biomedicine*, 14:1003–1013, 2010.
- [21] S. Petushi, F. U. Garcia, M. M. Haber, C. Katsinis, and A. Tozeren. Large-scale computations on histology images reveal grade-differentiating parameters for breast cancer. *BMC Medical Imaging*, 6(14), 2006.
- [22] D. W. Reed. On the pathological changes in Hodgkin’s disease, with special reference to its relation to tuberculosis. *Johns Hopkins Hosp Rep*, 10:133–396, 1902.
- [23] Scilab Enterprises and Scilab Consortium. *Scilab: Free and Open Source software for numerical computation*. Scilab Enterprises and Scilab Consortium, Digiteo, Paris, France, 2012.

- [24] O. Sertel, U. V. Catalyurek, G. Lozanski, A. Shanaah, and M. N. Gurcan. A combined computerized classification system for whole-slide neuroblastoma histology: Model-based structural features. In *International Conference on Medical Image Computing and Computer Assisted Intervention (MICCAI 2009)*, 2009.
- [25] O. Sertel, J. Kong, G. Lozanski, U. Catalyurek, J. H. Saltz, and M. N. Gurcan. Computerized microscopic image analysis of Follicular Lymphoma. In *Proceedings SPIE Medical Imaging*, pages 16–21, 2008.
- [26] C. Steidl, J. M. Connors, and R. D. Gascoyne. Molecular pathogenesis of Hodgkin’s Lymphoma: Increasing evidence of the importance of the microenvironment. *Journal of Clinical Oncology*, 29(14):1812–1826, 2011.
- [27] C. Sternberg. Über eine eigenartige unter dem Bilde der Pseudoleukämie verlaufende Tuberculose des lymphatischen Apparates. *Zeitschrift der Heilkunde*, 19(21-90), 1898.